Substrate-enhanced photothermal nano-imaging of surface polaritons in monolayer graphene

Fabian Menges,[1] Honghua Yang,[1,2] Samuel Berweger,[3] Anirban Roy,[2] Tao Jiang,[1,4] and Markus B. Raschke[1,a)]

[1)] *Department of Physics, Department of Chemistry, and JILA, University of Colorado at Boulder, Boulder, CO 80309, United States*

[2)] *Bruker Nano, 112 Robin Hill Road, Santa Barbara, California 93117, United States*

[3)] *Applied Physics Division, National Institute of Standards and Technology, Boulder, CO 80305, United States*

[4)] *MOE Key Laboratory of Advanced Micro-Structured Materials, and School of Physics Science and Engineering, Tongji University, Shanghai 200092, China*

(Dated: 10 March 2021)

Surface polaritons comprise a wealth of light-matter interactions with deep sub-wavelength scale confinement of electromagnetic modes. However, their nanoscale localized dissipation and thermalization processes are not readably accessible experimentally. Here, we introduce photothermal force microscopy to image surface plasmon polaritons (SPPs) in monolayer graphene through their non-radiative SiO_2 substrate dissipation. We demonstrate the real-space SPP imaging via photo-induced atomic force detection (AFM-IR), and from comparison with scattering-type scanning near-field optical microscopy (s-SNOM) imaging attribute the force response to substrate dissipation-enhanced thermal expansion. This work illustrates that nano-optical tip-sample induced dissipative forces facilitate a direct mechanical detection of surface polariton interactions with monolayer sensitivity.

[a)] Authors to whom correspondence should be addressed: fabian.menges@colorado.edu, markus.raschke@colorado.edu

The coupling of electromagnetic radiation to surface dipole excitations, in the form of surface polaritons (SPs) has recently sparked significant interest. Owing to their hybrid quasiparticle nature with strong light-matter coupling, SP modes confine electromagnetic energy down to the nanometer scale. Importantly, SPs provide a way to harness the rich physics of electromagnetic fields in deep sub-wavelength regimes, and to manipulate the macroscopic quantum properties of matter.[1–5] Both of these attributes hold significant promise for applications in areas such as thermoplasmonics[6,7], nano-bioimaging[8], nanoscale spectroscopy[5,9–11], optoelectronics, and quantum information transfer.[1,3,4]

Since the initial real-space observation of surface plasmon polaritons (SPPs) in graphene via scattering-type scanning near-field optical microscopy (*s*-SNOM),[5,9–12] a plethora of surface polaritons associated with electrons, phonons, excitons, and magnons have been investigated, including hyperbolic phonon polaritons (SPhPs) in hexagonal boron nitride (hBN),[13] exciton polaritons in vdW transition-metal dichalcalgognides (TMDs),[14] and SPP/SPhP modes in heterostructures such as hBN/graphene.[15] By providing the necessary high optical momentum in their near-field, sharp metallic scanning probe tips can simultaneously launch and probe these SP modes and have enabled rich spectroscopic insight into their nano-optical properties, propagation, local confinement, and interactions.[9–11,15–17]

On the other hand, comparably few studies have yet addressed the absorptive, nonradiative, and nanoscale localized dissipation and thermalization of these hybridized surface modes. Notably, photothermal scanning probe techniques have been used to visualize surface polaritons via local tip-induced excitations of photo-thermoelectric currents[18,19] and mechanical forces.[20–24] Photothermoelectric nanoscopy was used to image propagating surface plasmons in active graphene devices,[19] surface phonon polaritons in multilayer hBN were detected using photothermal nano-imaging techniques such as atomic-force microscope infrared spectroscopy (AFM-IR)[22], photothermal induced resonance (PTIR)[24], photo-induced force microscopy (PiFM)[20,21], and spectrally resolved peak-force infrared microscope (PFIR)[25]. However, in the limit of a monolayer material, nonradiative decay of the associated polaritons leading to a thermo-mechanical response has not yet been addressed.

In this work, we demonstrate real-space imaging of SPPs in monolayer graphene on silicon dioxide (SiO_2) through their dissipation and substrate-enhanced thermal expansion detected via photothermal AFM-IR. We directly compare AFM-IR to *s*-SNOM imaging of the same graphene flake and show that photothermal AFM enables the characterization of

non-radiative SPP decay based on direct local thermo-mechanical detection of the absorbed electromagnetic energy. While this non-radiative detection lacks the electromagnetic phase information accessible via *s*-SNOM, it can provide information about dissipation processes, such as the thermal decay of plasmons through optical phonon emission and electron-hole pair creation, and their subsequent thermal diffusion. AFM-IR therefore holds significant potential for real-space imaging of photo-induced thermo-physical processes in surface polariton systems.

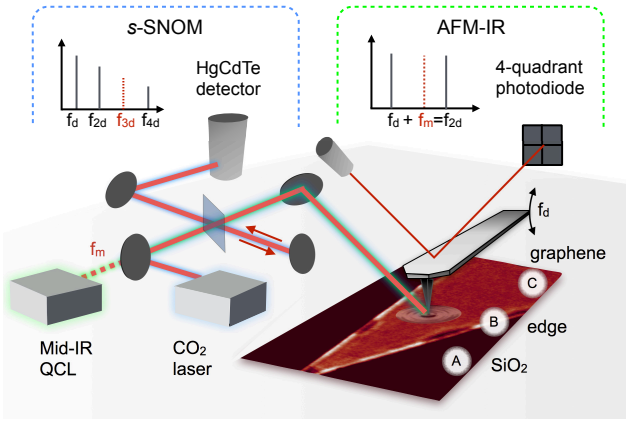

FIG. 1. Nanoimaging of graphene/SiO_2 surface plasmon polaritons with all-optical *s*-SNOM and photothermal AFM-IR. In *s*-SNOM the optical response of SPPs is detected interferometrically under continous-wave illumination (CO_2 laser), and lock-in demodulated at the third harmonic of the cantilever frequency (f_{3d}). In AFM-IR the SPPs are detected mechanically under pulsed-excitation using a mid-IR QCL tuned to the difference frequency (f_m) between the second and first mechanical mode of the cantilever.

Fig. 1 illustrates the combined *s*-SNOM and AFM-IR imaging of an exfoliated graphene flake (Graphene Industries) on a SiO_2/Si substrate. The IR laser beam is focused with an off-axis parabolic mirror onto the metallic AFM tip operating in dynamic mode feedback by driving and monitoring the cantilever motion at its fundamental resonance f_d. Surface polariton waves are launched by near-field momentum coupling from the metallic probe tip, propagate radially, reflect from the graphene SiO_2 edge, and interfere with the SP launched at the tip.[9–11] Depending on the detection mode, either tip-scattered light or a mechanical response of the tip-sample interaction is detected for *s*-SNOM and AFM-IR (Bruker/Anasys, NanoIR2s), respectively. In *s*-SNOM imaging, we use a CO_2 laser at 934 cm^{-1} ($\lambda = 10.7$ μm)

operating in continuous-wave (CW) mode, with interferometric two-phase homodyne near-field signal detection (HgCdTe detector, Kolmar Technologies). This provides real (Re) and imaginary (Im) part of the optical near-field and underlying local complex dielectric response function as established previously[11]. The far-field background is suppressed by lock-in demodulation at the third harmonic of the cantilever frequency (f_{3d}). For AFM-IR, the AFM operates in tapping mode with feedback at its fundamental cantilever mechanical mode ($f_d = 60$kHz). A sideband detection scheme is used to measure the cantilever deflection signal at the second cantilever mechanical mode $f_{2d} = 360$ kHz. This is achieved using a pulsed and wavelength tunable infrared laser (QCL, Daylight) with repetition rate tuned to the difference frequency between the second and the first mechanical mode of the cantilever $f_m = f_{2d} - f_d$, which gives rise to a cantilever sideband motion at f_{2d} due to nonlinear mixing.[26–28] AFM-IR detection in sideband mode relates to the force gradient rather than the total tip-sample interaction force, and is particular sensitive to thermal expansion mediated modulations of the tip-sample van der Waals force.[27,28] Both substrate-mediated, as well as tip-induced photothermal expansion, can cause forces proportional to the absorbed power.

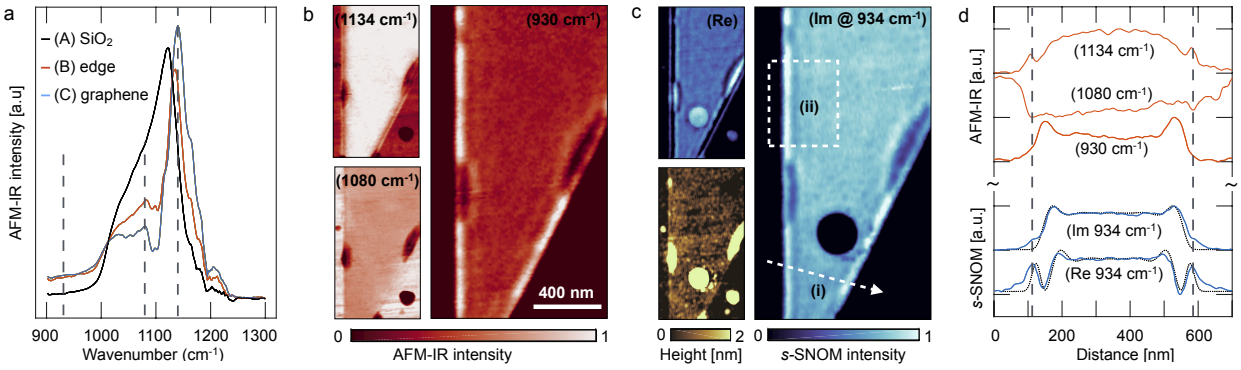

FIG. 2. (a) AFM-IR spectra at different sample locations (A,B,C) as indicated in Fig. 1, (b) AFM-IR images for three different IR excitation frequencies, (c) *s*-SNOM images of real (Re) and imaginary (Im) near-field signal at 934 cm^{-1} in comparison to AFM height, (d) Normalized line cuts along (dashed arrow in (c)) for the different signals.

Fig. 2(a) shows AFM-IR spectra from different regions of the sample. Within the tuning range of the QCL (900 – 1900 cm^{-1}) we resolve multiple peaks. On SiO_2, the strongest AFM-IR response is observed near 1100 cm^{-1}, corresponding to its infrared-active surface phonon polariton (SPhP) due to the asymmetric Si-O stretch vibration.[29] As AFM-IR detects a

thermo-mechanical expansion, the intensity of the AFM-IR signal is proportional to the light absorbed and the heat generated within the semi-infinite half-space below the tip. The graphene monolayer modifies the SPhP spectral response with the SiO_2 surface phonon resonance blue-shifting and narrowing, due to coupling between the substrate SPhP and the graphene SPP in accord with earlier reports.[30]

To characterize the distinct spatial variations, we performed real-space imaging of the graphene wedge for three different AFM-IR excitation energies (vertical dashed gray lines in the spectrum). These images [Fig. 2(b)] show strong correspondence of the graphene-substrate contrast in the spatial imaging to the spectral dependence [Fig. 2(a)]. In particular, we observe an enhanced AFM-IR intensity on graphene relative to SiO_2 for higher frequencies [Fig. 2(b), 1134 cm^{-1}] and find that this contrast is inverted at 1080 cm^{-1}. Notably, at a frequency of 930 cm^{-1}, i.e. detuned from the SiO_2 phonon mode (at 1100 cm^{-1}), we find SPP interference fringes with maximum intensity at the edges of the graphene wedge. As expected,[11] SPP interference fringes are also visible in the *s*-SNOM images [Fig. 2(c)] acquired with a CO_2 laser at 934 cm^{-1}, with the imaginary (Im) and real (Re) signal components as indicated.

To more quantitatively examine the relationship between the AFM-IR and *s*-SNOM signals, we extracted line cuts across different sample regions. Fig. 2(d) shows line cuts taken at location (i) marked by the dashed arrow in Fig. 2(c), with AFM-IR (top panels, red lines) and *s*-SNOM (bottom panels, blue line), and the dashed lines indicating the approximate edge positions extracted from the AFM heights. The lateral profiles of the AFM-IR signals not only show the material contrast between the graphene monolayer and the substrate, but clearly reveal interference fringes and a maximum intensity at the edge.

High-resolution images of the edge SPP interference pattern are shown in Fig. 3(a), with the complex-valued *s*-SNOM images and the measured AFM-IR amplitude images taken from region (ii) (dashed box) in Fig. 2(c). Averaged line profiles along the graphene edge are shown in Fig. 3(b), showing the SPP interference pattern for both *s*-SNOM and AFM-IR. As they are acquired at nearly the same frequency, the good agreement between the fringe spacing in the *s*-SNOM and AFM-IR line cuts away from the edge confirms that they probe the same SPP mode. However, the relative response on graphene in the absence of SPP interference differs significantly, and some notable differences in the details between AFM-IR and *s*-SNOM SPP interference pattern can be observed. In particular, the AFM-

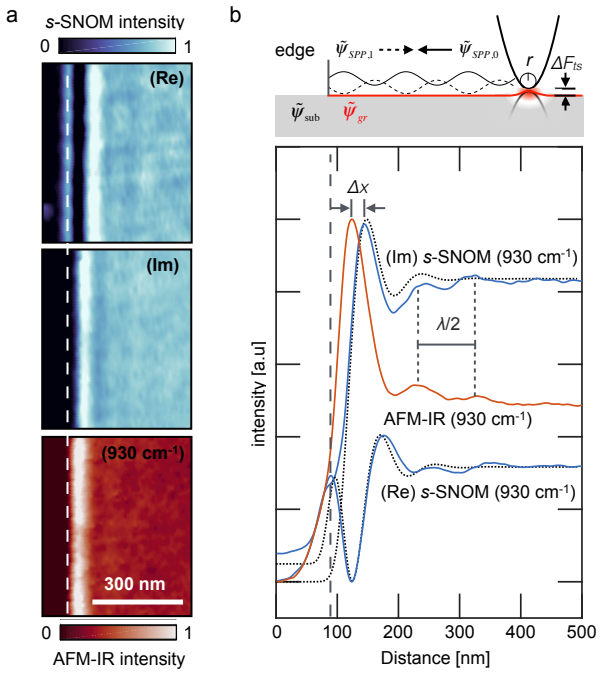

FIG. 3. Reflection and standing wave of the surface polariton at the graphene edge. (a) *s*-SNOM images of polariton reflection at the graphene edge plasmon with normalized real (Re) and imaginary (Im) part of the near-field *s*-SNOM signal at 934 cm^{-1} and the corresponding AFM-IR image of the reflected polariton mode at 930 cm^{-1}.(b) Averaged Cross-cut profiles of the polariton interference pattern taken across the dashed box indicated in Fig. 2(c).

IR signal shows a higher SPP fringe contrast across the graphene edge than the *s*-SNOM imaginary signal. This can be attributed to the fundamental differences in the physical contrast mechanism of the two techniques with their elementary steps of tip SPP launching and interferometric *s*-SNOM detection versus thermal expansion leading to the modulation of the tip-sample interaction force ($\Delta \mathrm{F}_{ts}$) as detected in the AFM-IR signal illustrated in Fig. 3(b).

In *s*-SNOM the SPP is detected in a process that is inverse to the SPP launching, where the tip acts as a local scattering center providing the necessary in-plane momentum to overcome the momentum mismatch between the SPP and free-space radiation. The tip thus scatters the local SPP field into propagating far-field, where the SPP amplitude A of the full complex-valued near-field signal is proportional to the local electrical field ($A \propto \tilde{E}$). To explain the observed SPP standing wave pattern in both *s*-SNOM and AFM-IR and to estimate the graphene mobility, we employ a phenomenological cavity model.[11,31] The local

electric field response of graphene underneath the tip Ψ_{gr} is formed as a superposition of the nonresonant dielectric contribution, the resonant local SPP $\tilde{\psi}_{\mathrm{SPP},0}$, and the relevant reflected SPP field $\tilde{\psi}_{\mathrm{SPP},1}$:

$$\Psi_{\mathrm{gr}} = \tilde{\psi}_{\mathrm{gr}} + \tilde{\psi}_{\mathrm{SPP},0} + \tilde{\psi}_{\mathrm{SPP},1}. \tag{1}$$

The reflected SPP field is given by $\tilde{\psi}_{SPP,1} = \tilde{R} \times \tilde{\psi}_{\mathrm{SPP},0} e^{-2Re(k_{\mathrm{SPP}})r(\gamma+1)}$ with decay constant γ, SPP wavevector $k_{\mathrm{SPP}} = 2\pi\lambda_{\mathrm{SPP}}^{-1}$, and complex valued scattering coefficient $\tilde{R}$. Lastly, we use a Gaussian weighting function Θ convolved with the spatial SPP field to account for the spatial averaging of the tip $\tilde{A}(r) = (\Psi * \Theta)(r)$. From our model [fits in Fig. 3(b)] we extract a decay constant of $\gamma = 0.4$ and a Fermi energy of $E_F = 0.35$ eV. This value of E_F confirms that we are operating in the regime where $2E_F > h\nu$, which prevents vertical optical transitions and the reduced damping thus enables long-range SPP propagation. The lack of optical absorption further prevents the generation of electron-hole pairs and photo-induced free carriers that can modify the carrier density. Our extracted decay constant $\gamma = \gamma_p + \gamma_{rad}$ is the superposition of Ohmic damping γ_p and the radial decay constant γ_{rad}. As in previous work[11], we estimate our radial decay constant to be $\gamma_{rad} = 0.13$, yielding $\gamma_p = 0.27$. This corresponds to a carrier mobility of $\mu \approx 700$ cm^2/V·s,[11,32] which is a low value for exfoliated graphene on SiO_2 and likely due to a long-term exposure of the sample to ambient conditions. Note that observed differences between the model and the detected spatial *s*-SNOM signal in Fig. 3(b) and Fig. 2(d) in the near-edge region arise from a local distortion of the evanescent field. At the edge of the flake, the SPP profile is complex and height (i.e., tip oscillation amplitude)-dependent, and an even fringe spacing in the spatial SPP pattern is not expected.[33] This further explains the difference in the spatial position of the first interference fringe in the AFM-IR and *s*-SNOM images.

The AMF-IR image at 930 cm^{-1} in Fig. 2(b) shows good qualitative correspondence to the *s*-SNOM images [Fig. 2(c)], with the same oscillation fringe spacing away from the edge. While *s*-SNOM detects the SPP excitations optically, the AFM-IR mechanically detects the thermal expansion following light absorption and SPP decay, giving rise to a measured amplitude that is proportional to the local SPP electrical field intensity $A \propto |E|^2$. The SPP decay can either occur within the graphene via ohmic losses, or via evanescent coupling of the SPP field to heavily damped SiO_2 phonon modes. However, due to the limited vertical thermal expansion of graphene itself due to the atomic monolayer thickness (≈ 0.35 nm) it

is likely that the thermal energy of either decay mechanism is ultimately transferred to the supporting substrate for the following reasons. First, the lateral thermal dissipation length of graphene was estimated from the electron cooling length to be > 200 nm according to a recent photothermal experiment.[19] A 200 nm dissipation length would limit the spatial resolution of AFM-IR to > 200 nm, significantly larger than our experimentally observed values. Second, a weak but discernible AFM-IR signal is observed with the tip immediately adjacent to the flake as seen in Fig. 3(b) and Fig. 2(d), which we attribute to substrate expansion itself. A photothermal expansion of the tip itself could also contribute to the contrast mechanism. Such a thermal dissipation of the SPP energy into the tip would nevertheless provide a conceptually equivalent decay pathway to substrate dissipation.

As seen in Fig. 2(b) and (d), the graphene shows a strong AFM-IR response at 1134 cm^{-1} with a strong near-edge fringe clearly visible. This indicates that the strong plasmon-phonon hybridization expected in this spectral range[30] efficiently couples the polariton energy into the substrate for thermal expansion while nevertheless enabling observation of the first fringe maximum near the flake edge. The excitation of a plasmon-phonon polariton hybrid mode would also mean that the initial heat generation would be highly confined to the graphene substrate interface, while for the substrate SiO_2 phonon polariton excitation absorbed electromagnetic energy becomes delocalized in the half space below the tip.

Overall, our observations suggests that ohmic dissipation in low-mobility graphene and subsequent heat transfer across the graphene SiO_2 interface is sufficient to render SPP detection possible via photothermal forces. The ability for real-space imaging of SPPs via AFM-IR thus provides spatial information about the non-radiative decay of deeply confined electromagnetic fields not attainable by all-optical detection methods.

In summary, we established substrate-enhanced photothermal SPP imaging with monolayer sensitivity comparing AFM-IR and IR *s*-SNOM for imaging SPPs on graphene/SiO_2. The results are consistent with previous work about the nature of AFM-IR photo-induced force microscopy signals in the mid-IR, indicating that photothermal expansion forces, rather than optical dipole-dipole forces are the main contributing physical mechanism.[27,28] Overall, the work represents a new way for direct spatial imaging of dissipative polariton modes and paves the way to thermal surface polaritonics. Controlling the photothermal response of surface polaritons appears as a potentially usefully approach to spatially pattern temperature fields on nanometer length and ultrafast time scales.

ACKNOWLEDGEMENTS

*Mention of product names is for informational purposes only and does not imply NIST's recommendation or endorsement. We acknowledge funding from the U.S. Department of Energy, Office of Basic Sciences, Division of Material Sciences and Engineering, under award no. DE-SC0008807. Fabian Menges gratefully acknowledges support of the Swiss National Science Foundation through project grant P300P2-174312, and the Branco Weiss Fellowship - Society in Science, administered by the ETH Zürich. T.J. is supported by the Shanghai Pujiang Talent Plan (No. 20PJ1414100) and the National Natural Science Foundation of China (62005198).

DATA AVAILABILITY

The data that supports the findings of this study are available within the article.

REFERENCES

[1]D. N. Basov, M. M. Fogler, and F. J. García de Abajo, "Polaritons in van der waals materials," Science **354** (2016).

[2]J. Kasprzak, M. Richard, S. Kundermann, A. Baas, P. Jeambrun, J. M. J. Keeling, F. M. Marchetti, M. H. Szymańska, R. André, J. L. Staehli, V. Savona, P. B. Littlewood, B. Deveaud, and L. S. Dang, "Bose–Einstein condensation of exciton polaritons," Nature **443**, 409–419 (2006).

[3]T. K. Hakala, A. J. Moilanen, A. I. Väkeväinen, R. Guo, J.-P. Martikainen, K. S. Daskalakis, H. T. Rekola, A. Julku, and P. Törmä, "Bose–Einstein condensation in a plasmonic lattice," Nat. Phys. **14**, 739–744 (2018).

[4]M. M. Fogler, L. V. Butov, and K. S. Novoselov, "High-temperature superfluidity with indirect excitons in van der Waals heterostructures," Nat. Commun. **5**, 4555 (2014).

[5]X. Liu, T. Galfsky, Z. Sun, F. Xia, E.-C. Lin, Y.-H. Lee, S. Kéna-Cohen, and V. M. Menon, "Strong light–matter coupling in two-dimensional atomic crystals," Nat. Photon. **9**, 30–34 (2015).

[6]Z. J. Coppens, W. Li, D. G. Walker, and J. G. Valentine, "Probing and controlling photothermal heat generation in plasmonic nanostructures," Nano Letters **13**, 1023–1028 (2013).

[7]A. Ahmadivand, N. Pala, and D. O. Güney, "Enhancement of photothermal heat generation by metallodielectric nanoplasmonic clusters," Opt. Express **23**, A682–A691 (2015).

[8]N. H. Ly and S.-W. Joo, "Recent advances in cancer bioimaging using a rationally designed raman reporter in combination with plasmonic gold," J. Mater. Chem. B **8**, 186–198 (2020).

[9]Z. Fei, A. S. Rodin, G. O. Andreev, W. Bao, A. S. McLeod, M. Wagner, L. M. Zhang, Z. Zhao, M. Thiemens, G. Dominguez, M. M. Fogler, A. H. C. Neto, C. N. Lau, F. Keilmann, and D. N. Basov, "Gate-tuning of graphene plasmons revealed by infrared nano-imaging," Nature **487**, 82–85 (2012).

[10]J. Chen, M. Badioli, P. Alonso-González, S. Thongrattanasiri, F. Huth, J. Osmond, M. Spasenović, A. Centeno, A. Pesquera, P. Godignon, A. Zurutuza Elorza, N. Camara, F. J. G. de Abajo, R. Hillenbrand, and F. H. L. Koppens, "Optical nano-imaging of gate-tunable graphene plasmons," Nature **487**, 77 –81 (2012).

[11]J. Gerber, S. Berweger, B. T. O'Callahan, and M. B. Raschke, "Phase-resolved surface plasmon interferometry of graphene," Phys. Rev. Lett. **113**, 055502 (2014).

[12]H. Yan, T. Low, W. Zhu, Y. Wu, M. Freitag, X. Li, F. Guinea, P. Avouris, and F. Xia, "Damping pathways of mid-infrared plasmons in graphene nanostructures," Nat. Photon. **7**, 394–399 (2013), arXiv:1209.1984.

[13]S. Dai, Z. Fei, Q. Ma, A. S. Rodin, M. Wagner, A. S. McLeod, M. K. Liu, W. Gannett, W. Regan, K. Watanabe, T. Taniguchi, M. Thiemens, G. Dominguez, A. H. C. Neto, A. Zettl, F. Keilmann, P. Jarillo-Herrero, M. M. Fogler, and D. N. Basov, "Tunable phonon polaritons in atomically thin van der Waals crystals of boron nitride," Science **343**, 1125–1129 (2014).

[14]F. Hu, Y. Luan, M. E. Scott, J. Yan, D. G. Mandrus, X. Xu, and Z. Fei, "Imaging exciton-polariton transport in $MoSe_2$ waveguides," Nat. Photon. **11**, 356–360 (2017).

[15]A. Woessner, M. B. Lundeberg, Y. Gao, A. Principi, P. Alonso-González, M. Carrega, K. Watanabe, T. Taniguchi, G. Vignale, M. Polini, J. Hone, R. Hillenbrand, and F. H. L. Koppens, "Highly confined low-loss plasmons in graphene–boron nitride heterostructures," Nat. Mater. **14**, 421–425 (2015).

[16]P. Alonso-González, A. Y. Nikitin, F. Golmar, A. Centeno, A. Pesquera, S. Vélez, J. Chen, G. Navickaite, F. Koppens, A. Zurutuza, F. Casanova, L. E. Hueso, and R. Hillenbrand, "Controlling graphene plasmons with resonant metal antennas and spatial conductivity patterns," Science **344**, 1369–1373 (2014).

[17]K.-D. Park, T. Jiang, G. Clark, X. Xu, and M. B. Raschke, "Radiative control of dark excitons at room temperature by nano-optical antenna-tip Purcell effect," Nat. Nanotechnol. **13**, 59–64 (2018).

[18]K. J. Tielrooij, L. Piatkowski, M. Massicotte, A. Woessner, Q. Ma, Y. Lee, K. S. Myhro, C. N. Lau, P. Jarillo-Herrero, N. F. van Hulst, and F. H. L. Koppens, "Generation of photovoltage in graphene on a femtosecond timescale through efficient carrier heating," Nat. Nanotechnol. **10**, 437–443 (2015).

[19]M. B. Lundeberg, Y. Gao, A. Woessner, C. Tan, P. Alonso-González, K. Watanabe, T. Taniguchi, J. Hone, R. Hillenbrand, and F. H. Koppens, "Thermoelectric detection and imaging of propagating graphene plasmons," Nat. Mater. **16**, 204–207 (2017), 1601.01977.

[20]A. Ambrosio, L. A. Jauregui, S. Dai, K. Chaudhary, M. Tamagnone, M. M. Fogler, D. N. Basov, F. Capasso, P. Kim, and W. L. Wilson, "Mechanical detection and imaging of hy-

perbolic phonon polaritons in hexagonal boron nitride," ACS Nano **11**, 8741–8746 (2017), 1704.01834.

[21]A. Ambrosio, M. Tamagnone, K. Chaudhary, L. A. Jauregui, P. Kim, W. L. Wilson, and F. Capasso, "Selective excitation and imaging of ultraslow phonon polaritons in thin hexagonal boron nitride crystals," Light Sci. Appl. **7** (2018), 10.1038/s41377-018-0039-4, 1711.04324.

[22]C. Ciano, V. Giliberti, M. Ortolani, and L. Baldassarre, "Observation of phonon-polaritons in thin flakes of hexagonal boron nitride on gold," Appl. Phys. Lett. **112**, 153101 (2018).

[23]J. Liu, S. Park, D. Nowak, M. Tian, Y. Wu, H. Long, K. Wang, B. Wang, and P. Lu, "Near-field characterization of graphene plasmons by photo-induced force microscopy," Laser Photonics Rev. **12**, 1800040 (2018).

[24]L. V. Brown, M. Davanco, Z. Sun, A. Kretinin, Y. Chen, J. R. Matson, I. Vurgaftman, N. Sharac, A. J. Giles, M. M. Fogler, T. Taniguchi, K. Watanabe, K. S. Novoselov, S. A. Maier, A. Centrone, and J. D. Caldwell, "Nanoscale mapping and spectroscopy of non-radiative hyperbolic modes in hexagonal boron nitride nanostructures," Nano Letters **18**, 1628–1636 (2018), 1710.10285.

[25]L. Wang, M. Wagner, H. Wang, S. Pau-Sanchez, J. Li, J. H. Edgar, and X. G. Xu, "Revealing phonon polaritons in hexagonal boron nitride by multipulse peak force infrared microscopy," Advanced Optical Materials **8**, 1901084 (2020).

[26]M. Tuteja, M. Kang, C. Leal, and A. Centrone, "Nanoscale partitioning of pclitaxel in hybrid lipid-polymer membranes," Analyst **143**, 3808–3813 (2018).

[27]B. T. O'Callahan, J. Yan, F. Menges, E. A. Muller, and M. B. Raschke, "Photo-induced tip-sample forces for chemical nano-imaging and spectroscopy," Nano Lett. **18**, 5499–5505 (2018).

[28]J. Jahng, E. O. Potma, and E. S. Lee, "Tip-Enhanced Thermal Expansion Force for Nanoscale Chemical Imaging and Spectroscopy in Photoinduced Force Microscopy," Anal. Chem. **90**, 11054–11061 (2018).

[29]O. Khatib, H. A. Bechtel, M. C. Martin, M. B. Raschke, and G. L. Carr, "Far Infrared Synchrotron Near-Field Nanoimaging and Nanospectroscopy," ACS Photonics **5**, 2773–2779 (2018).

[30]I. J. Luxmoore, C. H. Gan, P. Q. Liu, F. Valmorra, P. Li, J. Faist, and G. R. Nash, "Strong coupling in the far-infrared between graphene plasmons and the surface optical

phonons of silicon dioxide," ACS Photonics **1**, 1151–1155 (2014).

[31]Z. Shi, H. A. Bechtel, S. Berweger, Y. Sun, B. Zeng, C. Jin, H. Chang, M. C. Martin, M. B. Raschke, and F. Wang, "Amplitude- and phase-resolved nanospectral imaging of phonon polaritons in hexagonal boron nitride," ACS Photonics **2**, 790–796 (2015).

[32]M. Jablan, H. Buljan, and M. Soljačić, "Plasmonics in graphene at infrared frequencies," Phys. Rev. B **80**, 245435 (2009).

[33]J. H. Kang, S. Wang, Z. Shi, W. Zhao, E. Yablonovitch, and F. Wang, "Goos-hänchen shift and even-odd peak oscillations in edge-reflections of surface polaritons in atomically thin crystals," Nano Lett. **17**, 1768–1774 (2017).